Analysis of Potential Lifetime Extension Through Dynamic Battery Reconfiguration

Analysis of potential lifetime extension through dynamic battery reconfiguration

Albert Škegro, Changfu Zou, *Senior Member, IEEE*, Torsten Wik, *Member, IEEE*
CHALMERS UNIVERSITY OF TECHNOLOGY
412 96 Göteborg, Sweden
Tel.: +46 / (31) 772 10 00
E-Mail: {albert.skegro, changfu.zou, torsten.wik}@chalmers.se
URL: https://www.chalmers.se/

ACKNOWLEDGMENT

This work was funded by Mistra Innovation 23 under the project BattVolt. The computations were enabled by resources provided by Chalmers e-Commons at Chalmers.

***Index Terms*—Batteries, Battery management systems (BMS), Modular reconfigurable batteries, Lifetime, Switching cells.**

***Abstract*—Growing demands for electrification result in increasingly larger battery packs. Due to factors such as cell position in the pack and variations in the manufacturing process, the packs exhibit variations in the performance of their constituent cells. Moreover, due to the fixed cell configuration, the weakest cell renders the pack highly susceptible to these variations. Reconfigurable battery pack systems, which have increased control flexibility due to additional power electronics, present a promising solution for these issues. Nevertheless, to what extent they can prolong the battery lifetime has not been investigated.**

This simulation study analyzes the potential of dynamic reconfiguration for extending battery lifetime w.r.t. several parameters. Results indicate that the lifetime extension is larger for series than for parallel configurations. For the latter, the dominant factor is equivalent full cycles spread at the end of life, but resistance increase with age and the number of cells in parallel are also influential. Finally, for the former, the number of series-connected elements amplifies these effects.

I. INTRODUCTION

Contemporary transportation systems rely significantly on fossil fuels, whose consumption and associated tailpipe emissions not only damage ecosystems but are also main contributors to climate change and are unsustainable in the long run.

Electrification based on lithium-ion (Li-ion) batteries presents a promising way to mitigate this dependency. In order to attain their specifications, battery pack systems for electric vehicles (EV) are often comprised of many Li-ion battery cells. For instance, Tesla Model S Plaid has nearly 8000 cells [1], and a fully electric truck produced by Scania might have more than 20000 cells [2]. The battery management system (BMS), which accurately monitors the cells in the pack and keeps them within a safe (electric-thermal) operating window, is an indispensable component of such a large battery pack system.

In spite of this, large battery pack systems tend to be used inefficiently. As a result of variations in the manufacturing process and different local conditions in the pack, the cells do not age uniformly. A consequent large spread in cell capacities, or cell internal resistances, results in significant performance degradation for the fixed cell configuration with regard to capacity utilization and power output. Furthermore, the inability to disconnect cells implies that failure of a single cell not only presents a safety hazard but also renders the remaining healthy cells in the pack unusable.

Dynamic battery reconfiguration is a promising concept in this regard [3]. Essentially, battery pack systems allowing for dynamic reconfiguration, i.e., reconfigurable battery pack systems (RBSs), enable greater flexibility during the battery pack operation than conventional battery pack systems with a fixed cell configuration (FBSs). The reconfiguration is achieved by employing additional power electronics, e.g., by placing a certain number of switches around each cell, or group of cells, thus allowing for finer cell-level control and a range of potential benefits such as enhanced fault tolerance, prolonged battery pack life, customized output voltage, and mixing of cells having different properties.

Promising RBS applications include stationary energy storage systems (e.g., DC charging and microgrids [4]), as well as battery pack systems for electric vehicles (e.g., [5], [6]). Nevertheless, RBSs are not without challenges of their own. Although the additional power electronics enhances the operating flexibility, it also results in further electric and thermal losses. Moreover, the increased number of components also yields a higher total cost. Finally, increasing the number of switches for the purpose of improved controllability may render the system management highly complex.

The field of dynamic battery reconfiguration has been approached in several survey articles which have focused on the overview of the concept of dynamic battery reconfiguration [3], the comparison of existing RBS hardware configurations [7], and the review of control strategies in existing RBSs [8].

A systematic analysis of improvements gained by utilizing RBSs in place of FBSs is not only important for the motivation of RBSs but also presents a good initial step in designing an RBS solution. For instance, to what extent dynamic battery reconfiguration should be implemented will strongly depend on the lifetime extension of an RBS relative to the variations in its cells. No such analysis has been presented to the best of the authors' knowledge. Therefore, this paper aims to fill this gap by providing a simulation-based analysis with the following main contributions:

- A systematic method to create a set of cell ageing models from provided cell ageing data as an input to the study of the lifetime extension.
- A method for simulation-based analysis of the potential lifetime extension.
- Formulation of the lifetime extension for different RBS configurations.

The paper is organized as follows. Section II outlines the method used for the analysis, including the necessary definitions and the underlying assumptions. Section III presents the implementation. Section IV discusses the results for a publicly available dataset. Finally, Section V summarizes the findings.

II. Method

A. The system

In this paper, the term *parallel cell unit* (PU), denoting an electrical unit comprising N_p parallel-connected cells, is introduced. The PU can refer to either the *PU without reconfiguration*, i.e., the PU with a fixed cell configuration (FPU) or the *PU with ideal reconfiguration*, i.e., the reconfigurable PU (RPU). In the RPU, there is a switch adjacent to every cell which can engage or disengage the cell. Furthermore, each RPU is connected to a pair of switches, ensuring that the RPU can be engaged or bypassed.

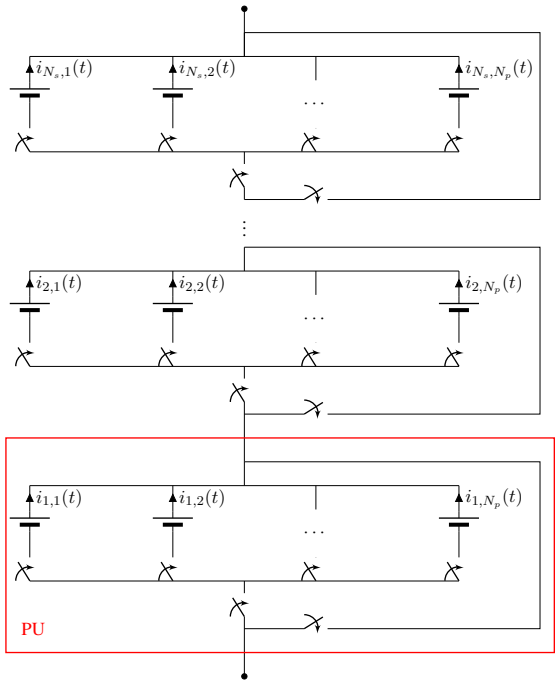

Fig. 1. A reconfigurable generalized module (RGM) with one of the reconfigurable parallel cell units (RPUs) enclosed in red, N_p representing the number of cells in the RPU, and N_s denoting the number of series-connected RPUs in the RGM.

Moreover, the term *generalized module* (GM) is used to denote an electrical unit comprising N_s series-connected PUs. The GM can refer to either the *GM without reconfiguration*, i.e., the GM with a fixed cell configuration (FGM) consisting of N_s series-connected FPUs or the *GM with ideal reconfiguration*, i.e., the reconfigurable GM (RGM) consisting of N_s series-connected RPUs.

RGM and its fundament RPU, depicted in Fig. 1, form the basis of the subsequent analysis.

B. Assumptions and conditions

In order to allow for the quantitative analysis, a considerable amount of full lifetime simulations for many cells is required. For this to be feasible, a set of assumptions is formulated to appropriately limit the scope of the study, or to simplify the simulation process without loss of generality.

Assumption 1. *The probability distribution functions (PDFs) of cell capacities at the beginning of life (BOL),*

denoted as $Q_{c,s}$, and of cell equivalent full cycles (EFCs) at the end of life (EOL), denoted as $EFC_{c,e}$, are known.

Remark. This assumption is the cornerstone of the subsequent analysis. Within the following simulation-based analysis, normal distribution with mean μ_s and variance σ_s^2 is chosen for the PDF of cell capacities at the BOL in line with experimental results obtained for a statistically significant number of Li-ion battery cells [9]. Hence, for the cell capacities at the BOL, normalised by the cell nominal capacity $Q_{c,nom}$, we have

$$\widetilde{Q}_{c,s} \sim \mathcal{N}\left(\mu_s,\, \sigma_s^2\right)\,, \tag{1}$$

where $\widetilde{Q}_{c,s}(t) = Q_{c,s}(t)/Q_{c,nom}$.

Furthermore, considering the PDF of cell EFCs at the EOL, normal distribution with mean μ_e and variance σ_e^2 is selected to keep the simulations comparable and simple, i.e.

$$EFC_{c,e} \sim \mathcal{N}(\mu_e,\, \sigma_e^2)\,. \tag{2}$$

However, any given distribution can equally be applied.

Assumption 2. *The thermal dynamics does not affect the lifetime difference between RBSs and FBSs.*

Remark. The cell temperature rise is expected to be small for the operating conditions. Hence, the cell temperatures are fixed and are assigned a value of 25°C, considering that it is a typically desired operating temperature for Li-ion battery cells.

Assumption 3. *The cell capacity degradation is dominated by cycling ageing.*

Remark. In order to assess cell ageing, cycling tests are often used. Based on a publicly available experimental cell ageing dataset from [10], within this analysis, it is assumed that the cells are in operation during most of their lives and that the difference in calendar ageing between RBS and FBS is negligible.

Assumption 4. *The cell capacity fade can be modelled as a linear function of cell EFC.*

Remark. In the initial stage of cell ageing, the cell capacity fade process can often be well approximated using a first-order polynomial [11]. Nevertheless, the cell undergoes different ageing processes during its lifetime, and accelerated and nonlinear ageing may appear when it approaches its EOL [12]. While leaving the study of different types of ageing models for future research, within this analysis, linear cell capacity fade trajectories, constructed based on cell ageing dataset [10], are considered. The data are shown in Fig. 2.

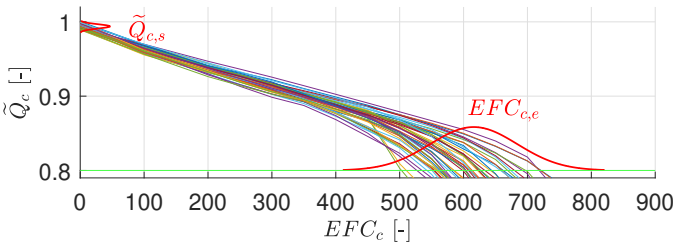

Fig. 2. Trajectories of Li-ion battery cell capacity fade with an illustration of the PDFs of normalised cell capacities at the BOL and of cell EFC at the EOL (in red). The data originate from [10].

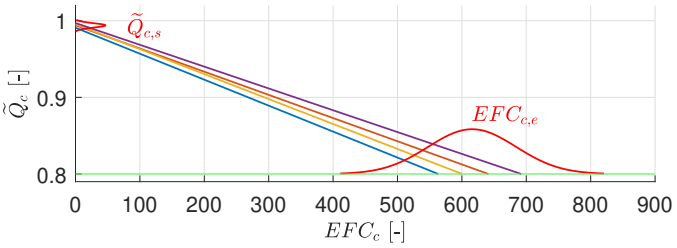

Fig. 3. Illustrative example of cell capacity fade trajectories for a PU consisting of four cells.

Consequently, the normalised cell capacity fade is modelled by connecting one realization of the distribution (1) with one realization of the distribution (2), as illustrated in Fig. 3.

Denormalisation by $Q_{c,nom}$ then results in

$$EFC_c(t) = a_c - b_c Q_c(t)\,, \tag{3}$$

where $a_c > 0$, $b_c > 0$, and $\widetilde{Q}_c(t) = Q_c(t)/Q_{c,nom}$.

Assumption 5. *The cell resistance increase is proportional to the cell capacity fade.*

Remark. This assumption builds upon experimental results [13]. A representative depiction of the relationship between the normalised cell capacity fade and the normalised cell resistance increase can be found in Fig. 4 where the normalised cell resistance $\widetilde{R}_c$ is defined as $\widetilde{R}_c(t) = R_c(t)/R_{c,nom}$.

Hence, $\widetilde{Q}_c$ and $\widetilde{R}_c$ are linked by the relationship

$$\widetilde{R}_c(t) = -k_{RQ}\widetilde{Q}_c(t) + l_{RQ}\,, \tag{4}$$

where $k_{RQ} > 0$, and $l_{RQ} > 0$.

Considering (4), the angle ρ between $\widetilde{R}_c = 1$ and the $\widetilde{Q}_c - \widetilde{R}_c$ lines from Fig. 4 can be calculated as

$$\rho_m = \arctan\left(1 - l_{RQ,m}\right)\,, \quad m = 1, 2, 3\,. \tag{5}$$

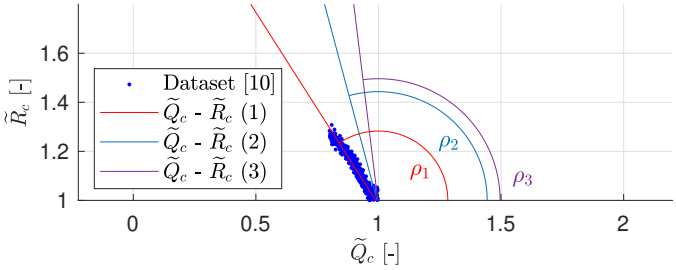

Fig. 4. The relationship between the normalised cell capacity fade and the normalised cell resistance increase (in dots for experimental data from [10]), along with the line of best fit for experimental data (1) and two perturbations for the simulation-based analysis ((2), (3)).

Denormalising (4) and combining it with (3) results in

$$R_c(t) = c_c + d_c EFC_c(t)\,, \tag{6}$$

where $c_c > 0$, $d_c > 0$.

Assumption 6. *The relationship between the open-circuit voltage (OCV) and the state-of-charge (SOC), namely the OCV-SOC curve, changes insignificantly during cell ageing.*

Remark. Within this analysis, the OCV-SOC relationship is, for the sake of simplicity, assumed to be constant, in line with the work in [14].

Assumption 7. *Full reconfiguration can be used to control cell usage such that all cells have the same capacity and SOC at the EOL.*

Remark. Consequently, when RBS reaches its EOL, its cells are at the same lower voltage limit v_{min}.

Assumption 8. *Losses in the RBS switches are negligible.*

Remark. Losses in the switches consist of switching losses and conduction losses. While switching losses are relatively low due to a low switching frequency commonly designed for RBSs [4], results from [15] indicate that conduction losses tend to contribute by less than 2% to the total RBS losses.

Condition. *Repeated cycles of discharging using constant current (CC) of one C-rate (1C) until the lower voltage limit is reached and charging using the constant current–constant voltage (CC–CV) protocol are applied. CC charging using 1C is executed until the upper voltage limit, followed by the CV phase until the charging current has decreased to C/30.*

Condition Remark 1. This simulation setup is in line with (even lower) C-rates expected in most EV operations (cf. [16]).

Condition Remark 2. Due to CC discharging and CC-CV charging, the polarization voltage transients are negligible in duration compared to both the discharge and the charge phase of the repeated cycles. Thus, the cell electric model reduces to a zero-order equivalent circuit model (ECM).

C. Definitions

Two approaches are used to define the EOL of PU. Approach 1 is based on commonly used reference performance testing procedures (e.g. [17]) and relates to usable capacity in EV applications. Approach 2 is focused on cell safety instead, implying that if the capacity of any cell in the PU is reduced below a certain threshold, it poses a safety hazard (cf. [18]). The latter approach naturally assumes knowledge of all cell capacities in the PU.

In subsequent definitions, index "i" refers to PU i in the GM ($i = 1, \ldots, N_s$), while index "j" refers to cell j in the PU ($j = 1, \ldots, N_p$). The negative discharge current sign convention applies throughout the calculations.

The PU 1C-discharge current is conveniently defined based on the cell 1C-discharge current:

$$i_{PU}^{1C} = i_c^{1C}\, N_p\,. \tag{7}$$

The PU nominal 1C-capacity is determined as the ampere-hour quantity obtained by cycling the FPU in the first CC discharge cycle with i_{PU}^{1C} from the higher voltage level v_{max} (corresponding to 100% SOC, starting at $t_{dis,1}^{s}$), to the lower voltage level v_{min} (reached at $t_{dis,1}^{e}$), in line with [19] and [20]:

$$Q_{PU,nom}^{1C} = -\int_{t_{dis,1}^{s}}^{t_{dis,1}^{e}} i_{PU}^{1C}\, d\tau\,. \tag{8}$$

The capacity trajectories of all PUs are assumed to be measured every cycle (hence, they are piecewise constant) and are calculated analogously to (8). For discharge cycles w (starting at $t_{dis,w}^{s}$ and finishing at $t_{dis,w}^{e}$) and $w+1$ (finishing at $t_{dis,w+1}^{e}$), i.e., for $\{t : t_{dis,w}^{e} < t < t_{dis,w+1}^{e}\}$, the *PU 1C-capacity* is defined as

$$Q_{PU}^{1C}(t) = -\int_{t_{dis,w}^{s}}^{t_{dis,w}^{e}} i_{PU}^{1C}\, d\tau\,. \tag{9}$$

In Approach 1, the *EOL of PU* is defined as the time instant when the PU 1C-capacity from (9) reaches 80 % of the PU nominal 1C-capacity, defined in (8):

$$t_{PU}^{e} = \min_{t}\ s.t.\ Q_{PU}^{1C}(t) \leq 0.8\, Q_{PU,nom}^{1C}\,. \tag{10}$$

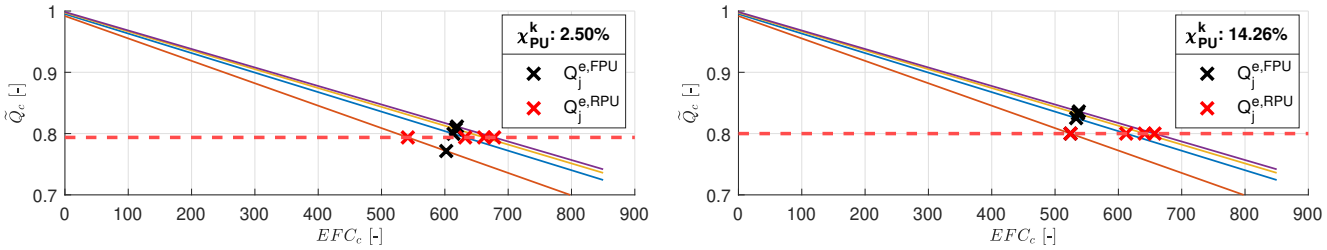

Fig. 5. Comparison of cell capacities at the EOL of FPU and RPU, each with four cells, evaluated for Approach 1 (left) and 2 (right).

In Approach 2, the *EOL of PU* is defined as the time instant when the first of the cells in the PU reaches the threshold of $80\,\%$ of the cell nominal capacity:

$$t^e_{PU} = \max_t \; s.t. \; Q_j(t) \geq 0.8\, Q_{c,nom}\,, \quad \forall j\,. \tag{11}$$

D. Analysis

The evaluation of potential lifetime extension through dynamic battery reconfiguration entails two steps. The first step necessitates quantifying the lifetime extension by employing RPU instead of FPU. This quantification is accomplished through a comparison of the cell EFCs at the EOL of FPU and RPU. These EFCs are calculated based on the respective cell capacities at the EOL using (3). This section therefore details how the cell capacities at the EOL of FPU and RPU are determined.

Subsequently, the second step quantifies the lifetime extension by utilizing RGM in place of FGM. As RPU is the fundament of RGM, results obtained in the first step provide the necessary input for this quantification.

1) PU analysis: For FPU, the full lifetime simulation is needed to determine the cell capacities at its EOL. For RPU, though, the cell capacities at its EOL can be calculated starting from the Assumptions. Hence, the idea is to repeatedly pairwise pick realizations of cell capacity at the BOL and cell EFC at the EOL (representatively depicted in Fig. 3); to determine cell capacities at the EOL of FPU from the full lifetime simulation; to determine cell capacities at the EOL of RPU through calculation (for both Approach 1 and 2); and finally, to evaluate the lifetime extension through dynamic battery reconfiguration, with an illustrative end-result depicted in Fig. 5.

a) FPU performance: The EOL of FPU is reached at t^e_{FPU}. The cell capacities at t^e_{FPU} are obtained from the full lifetime simulation:

$$Q_j^{e,FPU} \mathrel{\widehat{=}} Q_j\left(t^e_{FPU}\right)\,, \quad \forall j\,. \tag{12}$$

Subsequently, the EFC of FPU at t^e_{FPU} is obtained by summing the cell EFCs at t^e_{FPU} and using (3):

$$\begin{aligned} EFC^e_{FPU} &= \sum_{j=1}^{N_p} EFC_j^{e,FPU} \\ &= \sum_{j=1}^{N_p} \left(a_j - b_j Q_j^{e,FPU}\right) \end{aligned} \tag{13}$$

b) RPU performance: The EOL of RPU is reached at t^e_{RPU}. Assumption 7 indicates the equivalence of cell capacities and cell SOCs at t^e_{RPU}. The latter implies the equivalence of cell OCVs at t^e_{RPU}, i.e.:

$$Q_j^{e,RPU} \mathrel{\widehat{=}} Q_j\left(t^e_{RPU}\right) \mathrel{\widehat{=}} Q^{e,RPU}\,, \quad \forall j\,, \tag{14a}$$

$$z_j^{e,RPU} \mathrel{\widehat{=}} z_j\left(t^e_{RPU}\right) \mathrel{\widehat{=}} z^{e,RPU}\,, \quad \forall j\,, \tag{14b}$$

$$\Rightarrow v_{OC,j}^{e,RPU} \mathrel{\widehat{=}} v_{OC,j}\left(t^e_{RPU}\right) \mathrel{\widehat{=}} v_{OC}^{e,RPU}\,, \quad \forall j\,. \tag{14c}$$

Based on (14), $Q^{e,RPU}$ can now be calculated for both Approaches. For Approach 1, the intermittent goal is to reach two expressions for $v_{OC}^{e,RPU}$: firstly, by starting from (14a); secondly, by starting from (14b). The two expressions are subsequently equated. The resulting expression is solved numerically to produce $Q^{e,RPU}$.

Therefore, normalising (14a) by $Q_{c,nom}$, applying (4) and denormalising by $R_{c,nom}$ results in equivalence of cell resistances at t^e_{RPU}, i.e.,

$$R_j^{e,RPU} \mathrel{\widehat{=}} R_j\left(t^e_{RPU}\right) \mathrel{\widehat{=}} R^{e,RPU}\,, \quad \forall j\,. \tag{15}$$

Furthermore, by applying (14c) and (15) at t^e_{RPU}, in line with Condition Remark 2 we have

$$\begin{aligned} \sum_{j=1}^{N_p} v_{min} &= \sum_{j=1}^{N_p} \left(v_{OC}^{e,RPU} + i_j\left(t^e_{RPU}\right) R^{e,RPU}\right) \\ N_p v_{min} &= N_p v_{OC}^{e,RPU} + \sum_{j=1}^{N_p} \left(i_j^{e,RPU}\right) R^{e,RPU} \\ \Rightarrow i_j^{e,RPU} &= \frac{i_{PU}^{1C}}{N_p}\,, \quad \forall j\,. \end{aligned} \tag{16}$$

Rewriting (16) with consideration of (3) and (6) gives the first expression for $v_{OC}^{e,RPU}$:

$$v_{OC}^{e,RPU} = \alpha + \beta Q^{e,RPU}\,, \tag{17}$$

where

$$\alpha = v_{min} - i_{PU}^{1C}\left(c_j + a_j d_j\right)/N_p\,, \tag{18a}$$
$$\beta = i_{PU}^{1C} d_j b_j / N_p\,. \tag{18b}$$

Now, considering the last CC discharge cycle, starting at $t_{dis,last}^{s}$ and finishing at t_{PU}^{e} (i.e., $t_{dis,last}^{s} < t < t_{PU}^{e}$), the standard SOC equation for a cell in the PU is

$$z_j(t) = 1 + \frac{1}{Q_j(t)} \int_{t_{dis,last}^{s}}^{t} i_j(\tau) d\tau\,, \quad \forall j\ . \tag{19}$$

For the same cycle, applying Coulomb counting over the RPU with consideration of (10) gives

$$\begin{aligned} \sum_{j=1}^{N_p} \int_{t_{dis,last}^{s}}^{t_{RPU}^{e}} i_j(\tau) d\tau &= \int_{t_{dis,last}^{s}}^{t_{RPU}^{e}} \sum_{j=1}^{N_p} i_j(\tau) d\tau \\ &= \int_{t_{dis,last}^{s}}^{t_{RPU}^{e}} i_{PU}^{1C} d\tau \\ &= -0.8\, Q_{PU,nom}^{1C}\,. \end{aligned} \tag{20}$$

Evaluating (19) at t_{RPU}^{e}, summing over N_p, and applying (20) produces the second expression for $v_{OC}^{e,RPU}$:

$$v_{OC}^{e,RPU} = f\left(z^{e,RPU}\right) = f\left(1 - \frac{0.8}{N_p} \frac{Q_{PU,nom}^{1C}}{Q^{e,RPU}}\right)\,, \tag{21}$$

where f is the OCV-SOC curve from Assumption 6.

Finally, equating (17) and (21) results in

$$\alpha + \beta Q^{e,RPU} = f\left(1 - \frac{0.8}{N_p} \frac{Q_{PU,nom}^{1C}}{Q^{e,RPU}}\right)\ . \tag{22}$$

In (22), all parameters apart from $Q_{PU,nom}^{1C}$ and $Q^{e,RPU}$ are known. The former is obtained in line with (8) and the latter by numerically solving (22).

For Approach 2, $Q^{e,RPU}$ is, in line with (11), directly determined by setting $Q^{e,RPU} = 0.8\, Q_{c,nom}$.

For any Approach, the EFC of RPU at t_{RPU}^{e} is obtained by summing the cell EFCs at t_{RPU}^{e} and using (3):

$$\begin{aligned} EFC_{RPU}^{e} &= \sum_{j=1}^{N_p} EFC_j^{e,RPU} \\ &= \sum_{j=1}^{N_p} \left(a_j - b_j Q_j^{e,RPU}\right) \end{aligned} \tag{23}$$

c) PU lifetime extension: Ultimately, linking (13) and (23) allows the definition of the *PU lifetime extension in experiment k*:

$$\chi_{PU}^{k} = \left(\frac{EFC_{RPU}^{e}}{EFC_{FPU}^{e}} - 1\right) \cdot 100\,[\%]\,, \tag{24}$$

where an experiment refers to the simulation and calculations corresponding to one realization of cell aging models (cf. Fig. 3). The *statistics of PU lifetime extension* can be defined in terms of the sample mean $\bar{\chi}_{PU}$ and the sample standard deviation $s_{\chi_{PU}}$ of a set of N_{exp}^{PU} experiments, i.e.

$$\bar{\chi}_{PU} = \frac{1}{N_{exp}^{PU}} \sum_{k=1}^{N_{exp}^{PU}} \chi_{PU}^{k} \tag{25a}$$

$$s_{\chi_{PU}} = \sqrt{\frac{1}{N_{exp}^{PU} - 1} \sum_{k=1}^{N_{exp}^{PU}} \left(\chi_{PU}^{k} - \bar{\chi}_{PU}\right)^2} \tag{25b}$$

2) GM analysis: Since the same current passes through all PUs in the FGM, the FGM reaches its EOL when the first of its series-connected FPUs reaches its EOL. The *GM lifetime extension in experiment k* is therefore

$$\chi_{GM}^{k} = \left(\frac{\frac{1}{N_s} \sum_{i=1}^{N_s} EFC_{RPU,i}^{e}}{\min_i \left(EFC_{FPU,i}^{e}\right)} - 1\right) \cdot 100\,[\%]\,. \tag{26}$$

Similarly to (25), the *statistics of GM lifetime extension* can be defined in terms of the sample mean $\bar{\chi}_{GM}$ and the sample standard deviation $s_{\chi_{GM}}$ of a set of N_{exp}^{GM} experiments:

$$\bar{\chi}_{GM} = \frac{1}{N_{exp}^{GM}} \sum_{k=1}^{N_{exp}^{GM}} \chi_{GM}^{k} \tag{27a}$$

$$s_{\chi_{GM}} = \sqrt{\frac{1}{N_{exp}^{GM} - 1} \sum_{k=1}^{N_{exp}^{GM}} \left(\chi_{GM}^{k} - \bar{\chi}_{GM}\right)^2} \tag{27b}$$

III. Implementation

A. Data

1) Cell electrical model: The employed cell electrical model encompasses OCV, a series resistance R_0 and a single RC pair (consisting of polarization resistance R_1 and capacitance C_1). OCV is a function of SOC, while R_0, R_1, and C_1 are constant over the given temperature. The cell model parameters originate from [21].

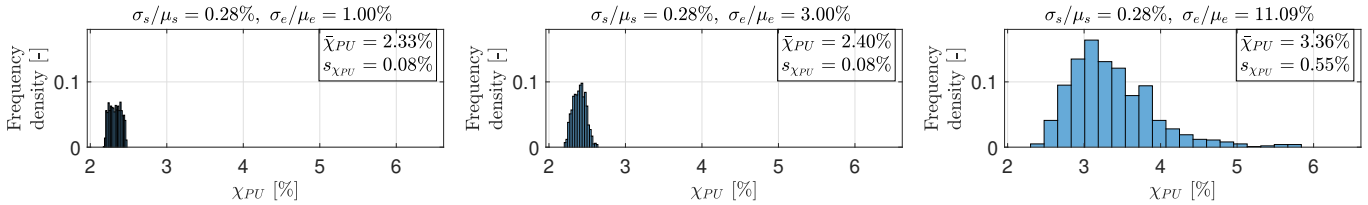

Fig. 6. Exemplified histograms of PU lifetime extension for the case of $N_p = 10$ and $\rho = 105.7°$, evaluated using Approach 1, normalised over N_{exp}^{PU}.

2) Cell ageing model: The used fraction of the cell ageing dataset, originating from [10], comprises data on 48 nickel-manganese-cobalt (NMC) cells. In [10], the cells were cycled using 1C-discharge and 1C-charge current alongside periodic characterization measurements, yielding cell capacity fade data as a function of EFC and cell resistance increase data (characterized at 50% SOC) as a function of EFC.

Within this analysis, the cell capacity fade data from [10] are normalised and fit to (1) and (2) using least-squares, resulting in the mean $\mu_{s,fit}$ and the standard deviation $\sigma_{s,fit}$ for the fitted normal distribution at the BOL and the mean $\mu_{e,fit}$ and the standard deviation $\sigma_{e,fit}$ for the fitted normal distribution at the EOL:

$$\begin{aligned} \widehat{\widehat{Q}}_{c,s} &\sim \mathcal{N}\left(\mu_{s,fit},\, \sigma_{s,fit}^2\right), \\ \widehat{EFC}_{c,e} &\sim \mathcal{N}\left(\mu_{e,fit},\, \sigma_{e,fit}^2\right), \end{aligned} \tag{28}$$

with

$$\begin{aligned} \{\mu_{s,fit}, \sigma_{s,fit}\} &= \{0.9939, 0.0028\}, \\ \{\mu_{e,fit}, \sigma_{e,fit}\} &= \{615.85, 68.28\}. \end{aligned} \tag{29}$$

Moreover, within this analysis, the cell resistance increase data from [10] are not directly used. Instead, the best least-squares fit is used to obtain k_{RQ} and l_{RQ} (cf. (4) and Fig. 4).

B. Experiment framework

Within this analysis, `SimScape` is used for cell modeling, while `MATLAB` and `Simulink` are used for conducting simulation experiments on the Linux-based computer cluster with 24 cores.

1) PU experiments: The parameters deemed to be able to influence the PU lifetime extension significantly are linked to cell manufacturing variations (σ_s), cell chemistry and usage characteristics (σ_e), cell chemical properties (ρ), and PU configuration (N_p).

Concerning σ_s and σ_e, two additional representative perturbations are selected alongside $\sigma_{s,fit}$ and $\sigma_{e,fit}$:

$$\frac{\sigma_s}{\mu_{s,fit}} \in \{0.1\%, 0.28\%\,\text{(fit.)}, 1\%\}, \tag{30a}$$

$$\frac{\sigma_e}{\mu_{e,fit}} \in \{1\%, 3\%, 11.1\%\,\text{(fit.)}\}. \tag{30b}$$

Moreover, two additional representative perturbations of ρ are selected alongside $\rho_1 \mathrel{\widehat{=}} \rho_{fit}$, evaluated using (5), and depicted in Fig. 4:

$$\rho \in \{124.5°\text{(fit.)}, 105.7°, 97.3°\}. \tag{31}$$

Finally, regarding N_p, the following values are selected:

$$N_p \in \{2, 4, 6, 8, 10, 12, 20\}. \tag{32}$$

Hence, the dimension of the simulation setup was $3^3 \times 7 = 189$ cases. The Monte Carlo method with $N_{exp}^{PU} = 1000$ experiments is applied for every case. At the start of every experiment, the cells have the same initial SOC of 50%. For every experiment, FPU performance is evaluated by using (10)–(13), while RPU performance is obtained by means of (14)–(23). Finally, statistics of PU lifetime extension is calculated on the basis of (24) and (25).

2) GM experiments: An additional factor deemed to be able to influence the GM lifetime extension significantly is linked to GM configuration (N_s).

Regarding N_s, the following values are selected:

$$N_s \in \{2, 3, \ldots, 9, 10, 15, \ldots, 200\}, \tag{33}$$

with the last entry reflecting the 800 V battery system.

Within a single case, for each N_s, a random sample of indices of size N_s is selected, with indices ranging between 1 and N_{exp}^{PU}. Performance indicators (13) and (23) corresponding to the selected indices are obtained. This procedure is repeated $N_{exp}^{GM} = 100000$ times. Statistics of GM lifetime extension is subsequently obtained using (26) and (27).

IV. Results And Discussion

Results for the PU lifetime extension χ_{PU} are, for all the 189 cases, obtained in terms of histograms of χ_{PU}, as exemplified in Fig. 6. In order to facilitate the comparison between different cases, the corresponding $\bar{\chi}_{PU}$ and $s_{\chi_{PU}}$ are also calculated for every histogram.

The influence of perturbation of the individual parameters (30)–(32) on χ_{PU} is presented in Fig. 7. Every data point in Fig. 7 corresponds to one of the 189 cases. Analogously, the results for χ_{GM} are, for the 189 cases and the 47 N_s values from (33), obtained in terms of histograms of χ_{GM} and the corresponding statistics $\bar{\chi}_{GM}$ and $s_{\chi_{GM}}$. The influence of perturbation of N_s on χ_{GM} is illustrated in Fig. 8. In contrast to Fig. 7, every line in Fig. 8 corresponds to one of the 189 cases.

A. Lifetime extension of RBSs

RBS has a significant potential to extend the lifetime of the battery pack systems with a fixed cell configuration (FBS) which are commonly used today. This is corroborated by each of the 189 investigated cases, as partially illustrated in Fig. 6 where χ_{PU} is positive in all experiments. Furthermore, the lifetime extension is particularly pronounced for the battery packs consisting of cells with a large EFC spread at the EOL and for battery packs comprising a large number of series-connected elements (namely large values of σ_e and N_s).

When evaluated using the safety-based Approach 2, $\bar{\chi}_{PU}$ is between $0.48\,\%$ and $24.31\,\%$, depending on the investigated case. Series-connecting the corresponding PUs results in an even higher lifetime extension. Specifically, for $N_s = 200$, corresponding to the $800\,\mathrm{V}$ battery system, the expected lifetime extension $\bar{\chi}_{GM}$ ranges between $2.62\,\%$ and $70.84\,\%$.

When evaluated using capacity-based Approach 1, $\bar{\chi}_{PU}$ ranges between $1.69\,\%$ and $4.46\,\%$. Correspondingly, for the $800\,\mathrm{V}$ battery system with $N_s = 200$, the highest expected lifetime extension is as large as $36.25\,\%$. Although inferior to the result obtained by evaluation for Approach 2, it is still a significant improvement over FBS. The difference in lifetime extension between the two Approaches is a strong indicator of the relevance of the dynamic battery reconfiguration not only for the lifetime extension of battery packs, but for their safety as well.

B. Effects of PU parameters

1) Effects of σ_s: Perturbations of σ_s, evaluated using both Approaches, show a marginal effect on χ_{PU} as both $\bar{\chi}_{PU}$ and $s_{\chi_{PU}}$ change insignificantly for an increase in σ_s (cf. Fig. 7a).

2) Effects of σ_e: In contrast to the marginal effect of σ_s, perturbations of σ_e, evaluated using both Approaches, have a pronounced effect on χ_{PU}. An increase in σ_e results in considerable increases in both $\bar{\chi}_{PU}$ and $s_{\chi_{PU}}$ (cf. Fig. 7b), in particular for Approach 2 where the increase is almost tenfold.

The PU lifetime extension in a single experiment χ_{PU}^k is illustratively determined by the relationship between black and red crosses in Fig. 5. In light of Fig. 2 and Fig. 3, it is reasonable to expect that perturbations of σ_s may affect the cell capacity fade trajectories less than perturbations of σ_e. Moreover, for increased σ_e, the cell EFC spread at the EOL of PU is wider, yielding a higher probability of one (or more) cell(s) in the PU having a cell capacity fade trajectory significantly different from the remaining cells. On the one hand, the cell capacity fade trajectories with significantly lower cell EFC at the EOL of PU than the remaining cells increase the risk of FPU reaching its EOL prematurely, thus rendering a higher $\bar{\chi}_{PU}$, especially for Approach 2. On the other hand, the cell capacity fade trajectories with significantly higher cell EFC at the EOL of PU than the remaining cells improve the FBS lifetime and reduce the effect of χ_{PU}, yielding a wider histogram of χ_{PU}^k (i.e., higher $s_{\chi_{PU}}$).

It is worth noting that, as σ_e increases, the histograms of χ_{PU} exhibit a right skew-symmetric behaviour with a pronounced "tail", as exemplified in Fig. 6. This is particularly important for χ_{GM}. The more pronounced the "tail" is, the higher the probability that the nominator in (26) is higher, yielding a more pronounced GM lifetime extension.

The considerable effect of σ_e on χ_{PU} mirrors the importance of the usage pattern of the RPU as a means of counteracting the variations in the cell manufacturing process and local temperature variations. In other words, using a proper control strategy, dynamic battery reconfiguration can be used to ameliorate the initial discrepancies between the cells and to serve as an effective long-term capacity balancing strategy.

3) Effects of ρ: Perturbations of ρ, evaluated using the two Approaches, result in different tendencies concerning χ_{PU}. For Approach 1, an increase in ρ results in a clear decrease of $\bar{\chi}_{PU}$ (cf. Fig. 7d), while the effect on $s_{\chi_{PU}}$ is negligible. Hence, an increase in ρ shifts the histogram of χ_{PU} to the right. For Approach 2, though, the perturbations in ρ have a negligible effect on both $\bar{\chi}_{PU}$ and $s_{\chi_{PU}}$.

The influence of the parameter ρ on χ_{PU} reflects the resistance variations between the individual cells. Although perhaps unexpected at first, this influence can

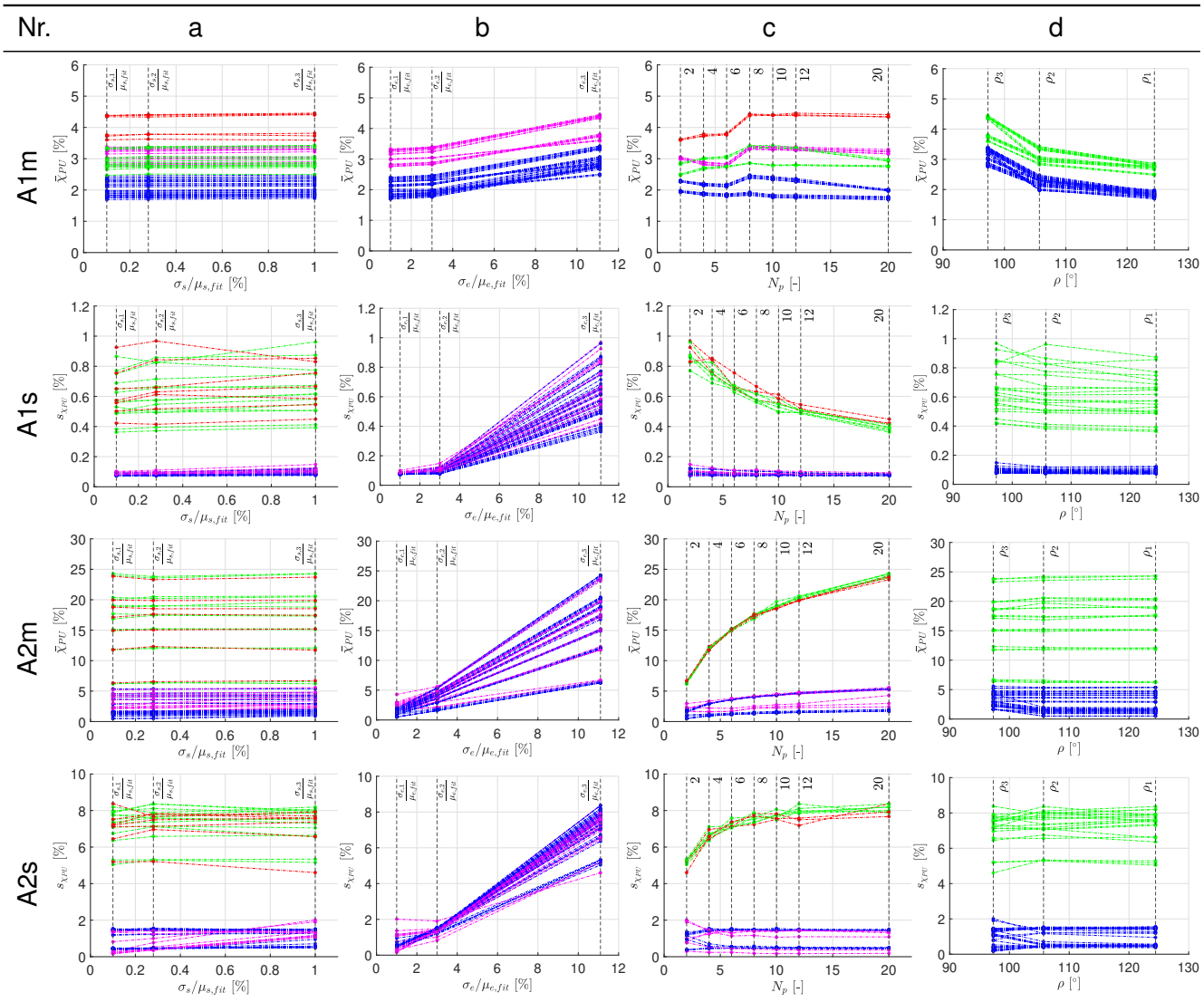

Fig. 7. Statistics of PU lifetime extension. Influence of perturbation of a) cell capacity spread at the BOL, b) cell EFC spread at the EOL, c) number of cells in the PU, d) cell resistance increase to cell capacity fade relationship. Influence on the mean (A1m and A2m) and the standard deviation (A1s and A2s) of the PU lifetime extension, evaluated for Approach 1 (A1m and A1s) and 2 (A2m and A2s). Green: Data for $\sigma_e = \sigma_{e,3}$. Magenta: Data for $\rho = \rho_3$. Red: Data for both $\sigma_e = \sigma_{e,3}$ and $\rho = \rho_3$. Blue: Remaining data.

be linked to the PU 1C-capacity, which is used for Approach 1 (cf. (10)). As lower values of ρ correspond to higher cell resistance values for a given cell capacity (cf. Fig. 4), the PU 1C-capacity is reduced accordingly due to the voltage drop over the resistance. The counterpart evaluation of χ_{PU} for Approach 2 uses the true cell capacity (cf. (11)) and is not affected by this.

4) Effects of N_p: Finally, perturbations of N_p, evaluated using the two Approaches, also result in different tendencies concerning χ_{PU}. For Approach 1, while the increase in N_p reduces or significantly reduces $s_{\chi_{PU}}$, no uniform trend for $\bar{\chi}_{PU}$ can be observed. An increase in N_p basically shrinks the histogram of χ_{PU}. In contrast to this, for Approach 2, an increase in N_p results in a clear increase of $\bar{\chi}_{PU}$ and a marginal effect on $s_{\chi_{PU}}$, apart from the cases which involve the highest σ_e-value from (30b), for which $s_{\chi_{PU}}$ increases as well.

An increase in the number of cells in the PU while keeping the same σ_s, σ_e, and ρ corresponds to an increase in the number of cell capacity fade trajectories in Fig. 3 while keeping the same $\tilde{Q}_{c,s}$ and $EFC_{c,e}$, which can be interpreted as more dense "sampling" within a single case. In light of Approach 1, an increase in N_p may result in improved averaging of the EFC of FPU, yielding only small changes in $\bar{\chi}_{PU}$ but a more accurate distribution (i.e., reduced $s_{\chi_{PU}}$). Possibly, the

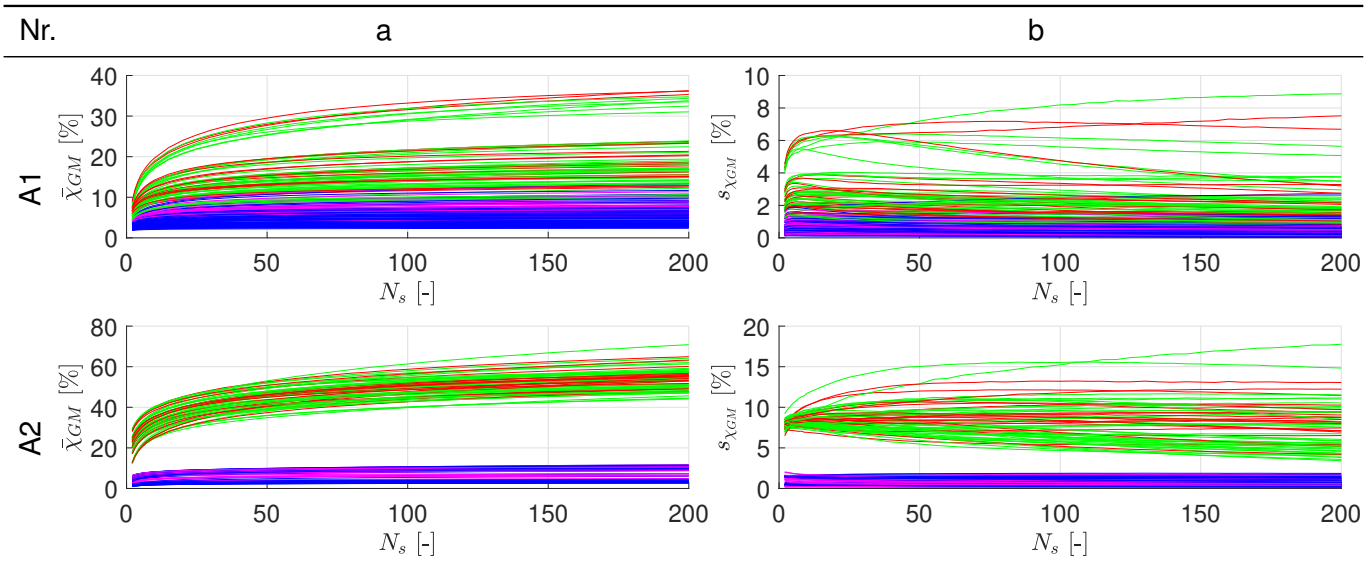

Fig. 8. Statistics of GM lifetime extension. Influence of the number of series-connected PUs on the mean (a) and the standard deviation (b) of the GM lifetime extension, evaluated for Approach 1 (A1) and 2 (A2). Green: Data for $\sigma_e = \sigma_{e,3}$. Magenta: Data for $\rho = \rho_3$. Red: Data for both $\sigma_e = \sigma_{e,3}$ and $\rho = \rho_3$. Blue: Remaining data.

histograms of χ_{PU} would eventually converge by further increasing N_p. In contrast, for Approach 2, evaluation shows that an increase in N_p considerably affects χ_{PU}, which can be explained in a manner analogous to that of an increase in σ_e.

The influence of perturbations of parameter N_p on χ_{PU} reflects the trade-off between the algorithm design and the PU configuration. On the one hand, provided that the commonly used 1C-capacity measurement is used for BMS algorithms, increasing the number of cells in the PU is not followed by the increased lifetime extension through dynamic battery reconfiguration. Increasing the number of cells in the PU may, however, lead to safety hazard (cf. Fig. 5 where one aged cell could operate below the safety threshold). On the other hand, provided that the cell capacities are perfectly known, the dynamic battery reconfiguration can maximize the capacity potential of the battery, which is especially pronounced when a cell whose capacity fade trajectory differs significantly from the other cells is added to the PU.

C. Effects of GM parameters

For all values of N_s from (33), both Approaches show that an increase in N_s results in an increase of $\bar{\chi}_{GM}$ (cf. Fig. 8a), which reflects the higher probability that some of the series-connected PUs will include cells which reach their EOL prematurely. No uniform trend for $s_{\chi_{GM}}$ could be observed though (cf. Fig. 8b). The reason for this stems from the underlying statistics of (26). The distribution of the resulting statistics (27) depends on the specific characteristics of the underlying finite-sample distribution of (26).

V. Conclusion

The field of RBSs is promising yet deficiently explored. Various researchers have tried to provide solutions that improve the RBS operation over FBS in a certain regard. This paper presents the first simulation-based analysis of the potential lifetime extension through dynamic battery reconfiguration. The system under study comprises series-connected units of parallel cells, where each such unit can be bypassed and each cell can be disconnected. A methodology to estimate the potential extension has been provided based on experimentally motivated assumptions on cell capacity fade, stochasticity, cell resistance increase, expressions derived for ideal reconfiguration, and extensive simulations.

The lifetime extension with respect to several parameters has been analyzed and discussed for a publicly available dataset from cell ageing experiments on NMC Li-ion cells. It has been shown that, for the investigated cell type, the lifetime extension for the $800\,\mathrm{V}$ battery system can be as high as 71%. The results indicate that the cell EFC distribution at the EOL and the number of series-connected units significantly impact the lifetime extension. Furthermore, the number of cells in parallel and the resistance increase with age can be influential as well, depending on the employed metrics.

REFERENCES

[1] M. Kane, "Watch Tesla Model S Plaid's Battery Get Opened And Described," *InsideEVs: Electric Vehicle News, Reviews, and Reports*, Oct. 13, 2021. [Online]. Available: https://insideevs.com/news/540380/tesla-models-plaid-battery-open/ (visited on Feb. 1, 2023).

[2] Volkswagen group, "Scania researches better batteries," Oct. 2, 2020. [Online]. Available: https://www.volkswagenag.com/en/news/2020/10/scania_research_batteries.html (visited on Feb. 10, 2023).

[3] W. Han, T. Wik, A. Kersten, G. Dong, and C. Zou, "Next-generation battery management systems: Dynamic reconfiguration," *IEEE Industrial Electronics Magazine*, vol. 14, no. 4, pp. 20–31, 2020.

[4] J. Engelhardt, J. M. Zepter, T. Gabderakhmanova, and M. Marinelli, "Efficiency characteristic of a high-power reconfigurable battery with series-connected topology," in *2022 International Power Electronics Conference*, 2022, pp. 2370–2376.

[5] N. Bouchhima, M. Schnierle, S. Schulte, and K. P. Birke, "Optimal energy management strategy for self-reconfigurable batteries," *Energy*, vol. 122, pp. 560–569, 2017.

[6] X. Huang, B. Jiang, and Y. Liu, "A reconfigurable battery supercapacitor hybrid energy system with active balancing for vehicle applications," in *2021 IEEE 19th International Power Electronics and Motion Control Conference (PEMC)*, 2021.

[7] S. Muhammad, M. U. Rafique, S. Li, Z. Shao, Q. Wang, and X. Liu, "Reconfigurable battery systems: A survey on hardware architecture and research challenges," *ACM Trans. Des. Autom. Electron. Syst.*, vol. 24, no. 2, 2019.

[8] Z. M. Pinter, D. Papageorgiou, G. Rohde, M. Marinelli, and C. Træholt, "Review of control algorithms for reconfigurable battery systems with an industrial example," in *2021 56th International Universities Power Engineering Conference (UPEC)*, 2021.

[9] S. Paul, C. Diegelmann, H. Kabza, and W. Tillmetz, "Analysis of ageing inhomogeneities in lithium-ion battery systems," *Journal of Power Sources*, vol. 239, pp. 642–650, 2013.

[10] W. Li, N. Sengupta, P. Dechent, D. Howey, A. Annaswamy, and D. U. Sauer, *Battery degradation prediction datasets and codes at ISEA*. [Online]. Available: https://git.rwth-aachen.de/isea/battery-degradation-trajectory-prediction (visited on Feb. 1, 2023).

[11] Y. Preger, H. M. Barkholtz, A. Fresquez, *et al.*, "Degradation of commercial lithium-ion cells as a function of chemistry and cycling conditions," *Journal of The Electrochemical Society*, vol. 167, no. 12, 2020.

[12] Y. Zhang, T. Wik, J. Bergström, M. Pecht, and C. Zou, "A machine learning-based framework for online prediction of battery ageing trajectory and lifetime using histogram data," *J. Power Sources*, vol. 526, p. 231 110, 2022.

[13] C. Pastor-Fernández, T. Bruen, W. Widanage, M. Gama-Valdez, and J. Marco, "A study of cell-to-cell interactions and degradation in parallel strings: Implications for the battery management system," *Journal of Power Sources*, vol. 329, pp. 574–585, 2016.

[14] Z. Song, X.-G. Yang, N. Yang, F. P. Delgado, H. Hofmann, and J. Sun, "A study of cell-to-cell variation of capacity in parallel-connected lithium-ion battery cells," *eTransportation*, vol. 7, p. 100 091, 2021.

[15] J. Engelhardt, J. M. Zepter, T. Gabderakhmanova, G. Rohde, and M. Marinelli, "Double-string battery system with reconfigurable cell topology operated as a fast charging station for electric vehicles," *Energies*, vol. 14, no. 9, 2021.

[16] E. Samadani, S. Farhad, S. Panchal, R. Fraser, and M. Fowler, "Modeling and evaluation of li-ion battery performance based on the electric vehicle field tests," *SAE Technical Papers*, vol. 1, 2014.

[17] J. Groot, *State-of-health estimation of li-ion batteries: Cycle life test methods*. Chalmers Tekniska Hogskola (Sweden), 2012.

[18] R. Teodorescu, X. Sui, S. B. Vilsen, P. Bharadwaj, A. Kulkarni, and D.-I. Stroe, "Smart battery technology for lifetime improvement," *Batteries*, vol. 8, no. 10, p. 169, 2022.

[19] F. Reuter, A. Baasner, J. Pampel, *et al.*, "Importance of capacity balancing on the electrochemical performance of $Li[Ni_{0.8}Co_{0.1}Mn_{0.1}]O_2$ (NCM811)/silicon full cells," *Journal of The Electrochemical Society*, vol. 166, no. 14, A3265, 2019.

[20] M. E. V. Team *et al.*, "A guide to understanding battery specifications," *Massachusetts Institute of Technology: Cambridge, MA, USA*, 2008.

[21] G. Plett, *ESC model toolbox*. [Online]. Available: http://mocha-java.uccs.edu/BMS1/CH02/ESCtoolbox.zip (visited on Feb. 15, 2023).